

Multiresolution Quality Inspection of Layerwise Builds for Metal 3D Printer and Scanner

Hui Yang¹

Industrial and Manufacturing Engineering, The Pennsylvania State University, University Park, PA 16802 e-mail: huiyang@psu.edu

Joni Reijonen

Advanced Manufacturing Tech, VTT Technical Research Center, 02044 Espoo, Finland e-mail: joni.reijonen@vtt.fi

Alejandro Revuelta

Advanced Manufacturing Tech, VTT Technical Research Center, 02044 Espoo, Finland e-mail: Alejandro.Revuelta@vtt.fi Automated optical inspection (AOI) is increasingly advocated for in situ quality monitoring of additive manufacturing (AM) processes. The availability of layerwise imaging data improves the information visibility during fabrication processes and is thus conducive to performing online certification. However, few, if any, have investigated the high-speed contact image sensors (CIS) (i.e., originally developed for document scanners and multifunction printers) for AM quality monitoring. In addition, layerwise images show complex patterns and often contain hidden information that cannot be revealed in a single scale. A new and alternative approach will be to analyze these intrinsic patterns with multiscale lenses. Therefore, the objective of this article is to design and develop an AOI system with contact image sensors for multiresolution quality inspection of layerwise builds in additive manufacturing. First, we retrofit the AOI system with contact image sensors in industrially relevant 95 mm/s scanning speed to a laser-powder-bed-fusion (LPBF) machines. Then, we design the experiments to fabricate nine parts under a variety of factor levels (e.g., gas flow blockage, re-coater damage, laser power changes). In each layer, the AOI system collects imaging data of both recoating powder beds before the laser fusion and surface finishes after the laser fusion. Second, layerwise images are pre-preprocessed for alignment, registration, and identification of regions of interests (ROIs) of these nine parts. Then, we leverage the wavelet transformation to analyze ROI images in multiple scales and further extract salient features that are sensitive to process variations, instead of extraneous noises. Third, we perform the paired comparison analysis to investigate how different levels of factors influence the distribution of wavelet features. Finally, these features are shown to be effective in predicting the extent of defects in the computed tomography (CT) data of layerwise AM builds. The proposed framework of multiresolution quality inspection is evaluated and validated using realworld AM imaging data. Experimental results demonstrated the effectiveness of the proposed AOI system with contact image sensors for online quality inspection of layerwise builds in AM processes. [DOI: 10.1115/1.4057013]

Keywords: multiresolution analysis, quality inspection, wavelet transformation, additive manufacturing, control and automation, sensing, monitoring and diagnostics

1 Introduction

Additive manufacturing (AM) offers an unparallel advantage to fabricate complex builds directly from digital designs. This, in turn, overcomes several production constraints (e.g., tooling cost, long lead time, lack of customization) in traditional subtractive and formative manufacturing. However, it is not uncommon that process variations cause internal defects in AM builds, which hamper the wide adoption of AM for safety critical industries (e.g., aerospace, nuclear, and healthcare sectors). Therefore, advanced imaging is increasingly invested to improve information visibility during the fabrication processes and cope with complexity in emergent AM technologies. For example, as shown in Fig. 1, optical images from digital single-lens reflex (DSLR) cameras were used to examine the recoating of powder beds, as well as surface finishes after the laser fusion [1,2]. Thermal images (2D and 3D) are captured to monitor the evolving dynamics of melt pools, which are critical to the melting and solidification process of laser fusion [3-5]. The postbuild computed tomography (CT) scans help characterize and estimate the defects of an AM build from the laser-powder-bed-fusion (LPBF) process.

The availability of layerwise imaging data has fueled increasing interests to design and develop automated optical inspection (AOI)

systems for online certification of AM builds. Although there are significant advances in the design of different AM sensing modalities (e.g., DSLR camera, spectrometer, acoustic emission, melt-pool sensing) in the state of the art, few, if any, have investigated the high-speed scanning of both pre-fusion spread powder and postfusion lasered surfaces with contact image sensors (CIS) (i.e., originally developed for document scanners and multifunction printers) for in situ quality monitoring of AM processes. Hence, we made an attempt to retrofit the AOI system with CIS to a metal LPBF machine. This contact image sensor is mounted on the re-coater arm to collect in situ images from each layer of the AM process.

Realizing the full potential of imaging data depends highly on the development of new analytical methods for layerwise quality inspection in the AOI system. Indeed, dealing with imaging data is a general problem facing both next-generation innovation practices for quality engineering in advanced manufacturing. Traditional statistical quality control is more concerned about univariate monitoring of a single feature or joint monitoring of multiple features, but is limited in the ability to handle complex-structured imaging data. In addition, layerwise AM images show complex patterns and often contain hidden information that cannot be revealed in a single scale. A new and alternative approach will be to analyze these intrinsic patterns with multiscale wavelet lenses. Multiresolution analysis is conducive to improving the effectiveness of image-based quality inspection in the AOI system. Complex imaging data can then be examined in multiple scales to extract salient features that are not directly observable in a single scale.

¹Corresponding author.

Manuscript received November 2, 2022; final manuscript received February 19, 2023; published online June 7, 2023. Assoc. Editor: Jaydeep Karandikar.

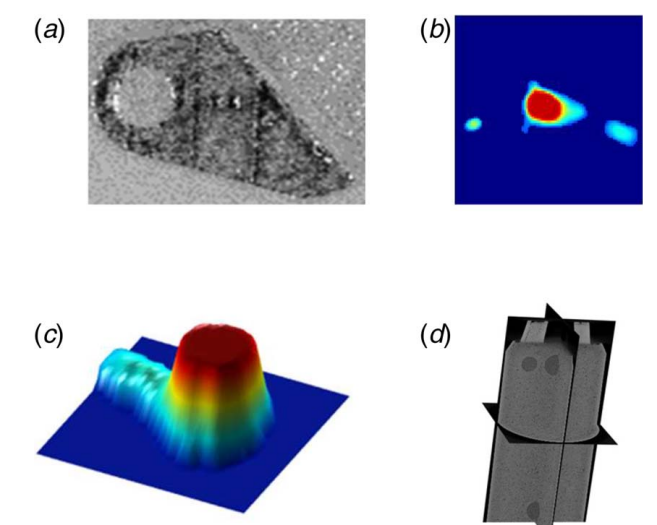


Fig. 1 Examples of high-dimensional imaging profiles in AM: (a) optical image of an AM laywise build, (b) 2D visualization of a melt pool with spatters, (c) 3D visualization of a melt pool, and (d) CT scan

Therefore, this article presents the design and development of an AOI system with CIS for multiresolution quality inspection of layerwise builds in additive manufacturing. Our first contribution is the retrofitting of contact image sensors to a LPBF machine with attractive features such as (1) sufficiently high 1200 dpi resolution, (2) significant (184 mm) scanning width, and (3) industrially relevant 95 mm/s scanning speed that does not need to reduce the productivity of the printer. As shown in Fig. 2, this enables the collection of rich layerwise images from pre-fusion recoating powder beds, as well as post-fusion surface finishes. Then, we run a design of experiments to fabricate nine parts in one build plate under a variety of factor levels (e.g., gas flow blockage, re-coater damage, laser power changes). Furthermore, layerwise images are pre-preprocessed for alignment, registration, and identification of regions of interests (ROIs) of these nine parts. Notably, we propose the wavelet transformation to analyze ROI images in multiple scales and further extract salient features that are sensitive to process variations, instead of extraneous noises. Finally, we perform the paired comparison analysis to investigate how different levels of factors influence the distribution of wavelet features. In addition, these features are shown to be effective in predicting the extent of defects in the CT data of layerwise AM builds. The proposed framework of multiresolution quality inspection is evaluated and validated using real-world AM imaging data. Experimental results demonstrated the effectiveness of the proposed AOI system with contact image sensors for online certification of layerwise builds in AM processes.

2 Research Background

Quality assurance and quality control (QA/QC) are indispensable in the development of new additive manufacturing technologies. AM is well known for the layer-by-layer fabrication of complex parts directly from digital designs. If a defect is not detected in a layer during the AM process, it will be sealed inside the build as subsequent layers are deposited. Although postbuild CT can effectively identify such embedded defects, it will then be too late to make any corrections. In situ sensing overcomes such drawbacks and provides an opportunity to monitor and detect the defect on the fly [6]. Therefore, the development and implementation of in situ sensing capabilities for AM QA/QC have fueled increasing interests in the community of AM researchers and machine providers.

For example, National Institute of Standards and Technology (NIST) researchers developed the Additive Manufacturing Metrology Testbed (AMMT) that integrates high-resolution cameras for melt pool monitoring during the AM process [7,8]. CIMP-3D at Penn State designed a multisensor monitoring system (i.e., including high-resolution cameras, optical process emissions, acoustic sensors, thermal imaging and melt-pool sensors) that can be retrofit into a variety of commercial AM systems, e.g., EOS M280, 3D Systems ProX 200, and GE M2 machines [9,10]. In addition, Edison Welding Institute (EWI) developed an Open Architecture LPBF platform that is instrumented with a variety of sensors such as coaxial infrared thermal cameras, photodetector spectrometer, digital cameras, acoustic sensors, and laser interferometer [11]. See more details on in situ AM sensing in recent review articles by Yang et al. [12] and McCann et al. [13].

Although there are significant advances to develop in situ sensing systems, few have investigated the high-speed scanning of both prefusion spread powder and post-fusion lasered surfaces with CIS (i.e., originally developed for document scanners and multifunction printers) for AM quality monitoring. In the state of the art, Lu et al. and Le and Seita have considered the use of consumer-grade CIS sensors for in-line characterization of powder bed defects and prediction of build density [14,15]. However, CIS sensors from consumer grade flatbed scanner yield slow speeds, i.e., around 7 mm/s for 1200 dpi images, and 0.2 mm/s for 4800 dpi. Thus, it takes approximately 1 min to acquire an image per layer. Little has been done to investigate the high-speed CIS sensors with industrially relevant 95 mm/s scanning speed that does not need to reduce the productivity of the printer. Therefore, this article focuses on the design and retrofitting of high-speed CIS sensors into a LPBF

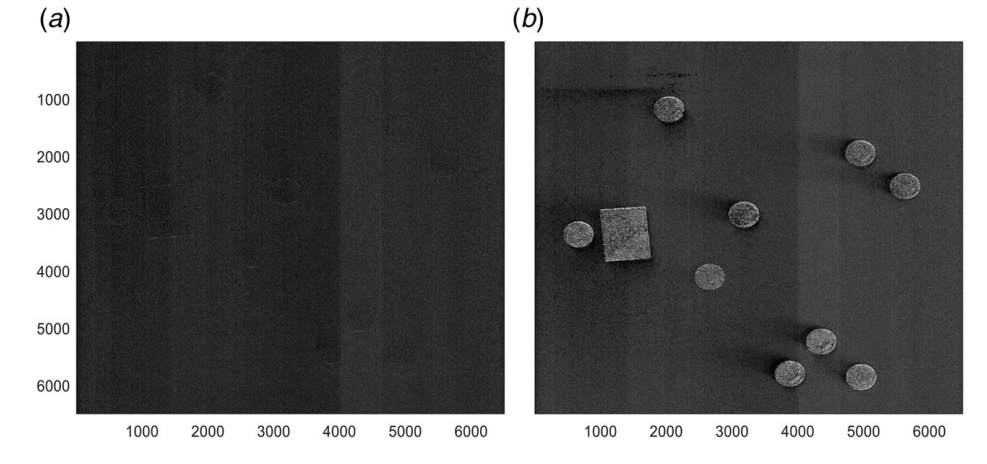
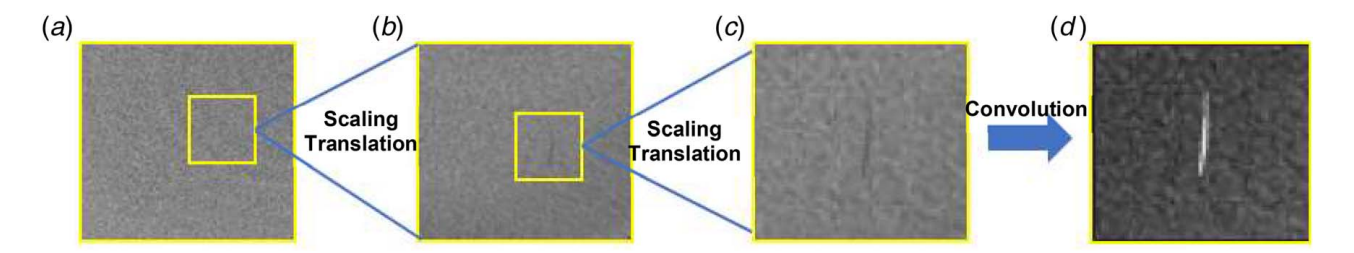


Fig. 2 Examples of imaging profiles collected by the contact image sensors from (a) prefusion recoating powder beds and (b) post-fusion surface finishes at each layer of LPBF-AM



ig. 3 Multiresolution analysis of imaging data through mathematical transformations (i.e., scaling and convolution)

machine. Our objective is to evaluate the capability of high-speed and high-resolution CIS sensing and data acquisition systems for QA/QC in the AM processes.

With the increasing adoption of imaging sensors, large amounts of layerwise imaging data are proliferated during AM processes. Often, these images contain nonlinear, nonstationary, and irregular patterns that provide hidden information pertinent to the progressive formation of defects. Realizing the full potential of imaging data for AM QA/QC depends on the design and development of new analytical methods and tools. As such, recent years have witnessed an increasing amount of research works on image processing and machine learning for AM defect prediction and statistical quality monitoring. For example, Caggiano et al. investigated machine learning approaches for image processing and online defect detection in metal-based AM processes [16]. Yao et al. performed a multifractal analysis of layerwise images for the characterization of defect patterns in the LPBF-AM process [17,18]. Kan and Yang derived the low-dimensional network representation of layerwise images and then leveraged network metrics for anomaly detection [19]. Deep neural networks are also used to learn the ROI of layerwise images for the prediction of AM defects [20,21]. Liu et al. developed an additive Gaussian process model of layerwisedependent images and then constructed the statistical control charts for monitoring the AM processes [22]. Yang et al. investigated the tensor decomposition of melt-pool images into lowdimensional profiles, and then leverage statistical control charts to monitor melt-pool variations in the metal-based AM process [23]. Liu and Yang also simulated the emission of photons in the LPBF process for statistical estimation and modeling of the multimodal probability distribution function of a melt pool [24]. However, most of existing works tend to focus on image processing and analysis in a single scale. It is not uncommon that defect characteristics are often buried in such a single-scale view. Little has been done to investigate multiresolution analysis of layerwise images for in situ characterization of defect patterns, as well as in-process quality monitoring.

As shown in Fig. 3, porosity defects may not be discernible by visual inspections in the original scale, but are more salient when delineated in different resolutions. It is worth noting that multiresolution analysis is not just limited to magnification, but rather are performed with a series of mathematical operations, e.g., scaling

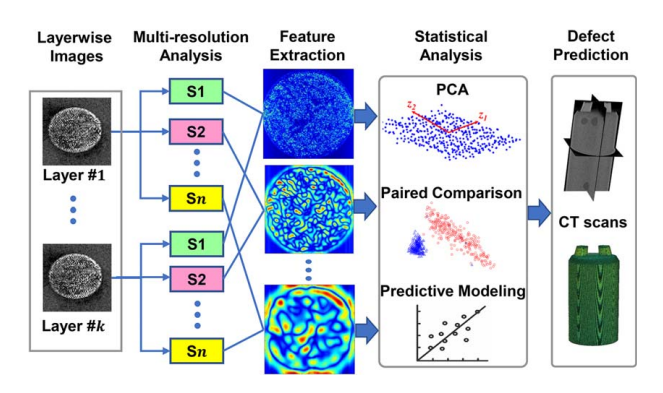


Fig. 4 Multiresolution quality monitoring of AM

 $s(x) \rightarrow s(x/a)$, translation $s(x) \rightarrow s(x-b)$, or convolution $s(x) \rightarrow s(x)$ $\times \psi(x)$ [25]. For example, wavelet transform leverages scaling, translation, and convolution with compact-supported waves to delineate both spatial locations and frequency information for multiresolution analysis of hidden defects. Delineating such hidden information helps to improve the effectiveness of defect identification and statistical monitoring frameworks. Conventional frequency analysis, e.g., Fourier transform, extracts frequency information in the image but lacks spatial location information [26]. Wavelet transform provides a better characterization of AM images by extracting time-varying and spatially dependent spectral components across different scales. Wavelet transform resolves the spatial-frequency information using a set of compactly supported wavelet functions [27], thereby providing a multiresolution representation for AM process monitoring. As opposed to image learning and modeling in the original scale, new multiresolution methods are urgently needed to handle quality inspection of layerwise builds in AM.

3 Research Methodology

This article presents the integration of CIS sensors into a LPBF-AM machine, and further develops a new multiresolution inspection approach of in situ layerwise images for quality monitoring of AM process, as opposed to the traditional inspection schemes in a single scale. As shown in Fig. 4, the present investigation is embodied with three components: (1) multiresolution transformation of layerwise images into wavelet scales S1, S2, ..., Sn; (2) multiscale feature extraction to characterize nonlinear and nonstationary patterns in wavelet scales that are sensitive to the variations of process factors; and (3) statistical analysis and defect prediction for AM quality assurance. Principal component analysis (PCA) is leveraged to reduce the dimensionality of wavelet features and build a sparse linear mix-effects model that prevents the overfitting, while maintaining the prediction performance. Postbuild CT scans are utilized to quantify and measure the level of defects in the AM parts, which serves as the response variable for the predictive modeling. These components are eventually integrated into the framework of multiresolution inspection to realize the full potential of CIS sensors for in situ AM monitoring and quality assurance.

3.1 Retrofit the Contact Image Sensors Sensing System to **Aadditive Manufacturing Machines.** The machine employed is a SLM125 from SLM Solutions GmbH, with a 400 W laser and a building platform of 125 × 125 mm. As shown in Fig. 5, the CIS is mounted on the re-coater arm, which covers the 183 mm scan width and supplies the layerwise images in the resolution of 1200 dpi (21 μ m/pixel). The focal distance of the sensor is 0.9 mm. Twosided RGB LED lighting is integrated on the CIS sensor unit. The CIS is attached to the SLM125 re-coater using brackets: both scanning head and control electronics. Power and data signal are routed through a sealed passthrough aperture in the back of the building chamber. The CIS control electronics are connected to the principal component (PC) using USB3.0. The recoating speed has been adjusted to acquire an image with a 1:1 aspect ratio and match with the scans in the high speed of 95 mm/s (i.e., relevant for industrial scale 3D printing). The control PC is connected to the SLM125

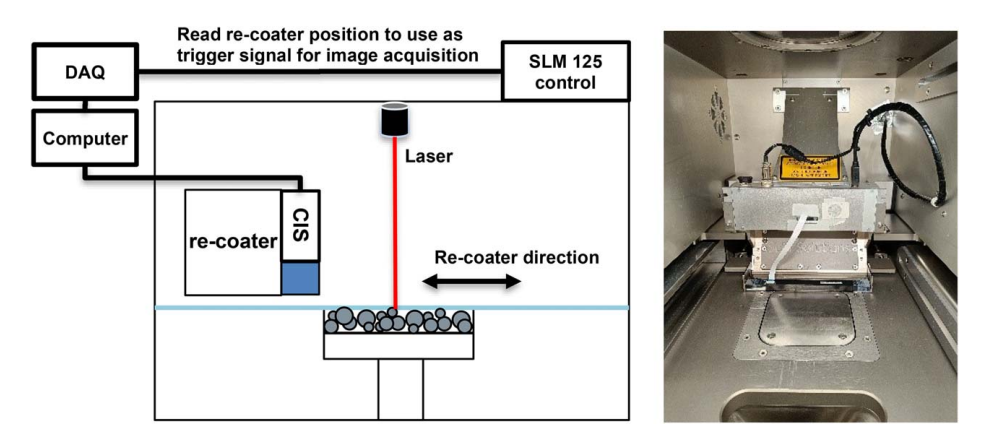


Fig. 5 Schematic diagram and CIS sensor integration for layerwise scanning in the SLM125 AM machine

CAN bus using a Kvaser interface for the data acquisition, reading the re-coater position in real time and triggering the powder bed scanning every time the recoating process takes place.

Registration and Region Segmentation. CIS sensor is configured to scan the powder bed before and after the laser fusion of each layer. Therefore, at each layer, two images are collected, one is from the powder bed before the laser fusion and the other is from surface finishes after the laser fusion, as shown in Fig. 2. However, because CIS sensors are moving back and forth, two images are 180 deg flipped and not well aligned at each layer. Although the control system is configured for 1:1 alignment, motors often cannot precisely move CIS sensors to the exact locations. Also, exact triggering of the system depends on the communication frequency of the positioning messages in the CAN bus. These images are collected under changing positions that vary the sensor perspective and the scene angle. This leads to a small level of uncertainty across all layers. Therefore, image registration cannot be uniformly done (i.e., consistent shifts of x- and y-coordinates) to align the preand post-fusion images at each layer. For example, Fig. 2(a) shows the traces of circular parts from the previous layer in the prefusion image, but their locations are misaligned with those parts in the post-fusion image in Fig. 2(b).

Hence, the first step is to perform image registration to align preand post-fusion images, which helps perform a joint analysis of each layer. In this investigation, the post-fusion image is designated as the reference image (or the fixed image) and the pre-fusion image is the moving one. The objective of image registration is to apply geometric transformations (e.g., translation, rotation, cropping, resizing) to the moving image so that it can be well aligned with the reference. Nonetheless, the challenge lies in the scene differences between these two images. Our experiments showed that traditional intensity-based registration algorithms cannot converge and fail to effectively align these two images. Alternatively, we propose to leverage the features (i.e., circular traces and objects available in both images) to perform feature-based registration. This process involves four steps: detect features, extract features, match features, and then apply geometric transformations to align features and images. As shown in Fig. 6, feature-based image registration effectively handles the misalignment issue and combines both images to create a composite view. Here, the pre-fusion image of powder layer before solidification is substracted from post-fusion image to obtain an enhanced contrast and improve the signal-to-noise ratio that is otherwise difficult to obtain from a single image. As a result, we can extract the ROIs for all parts from C1, C2, ..., to C10, which will be used for wavelet analysis in the next section. Note that the focus of this article is on the multiresolution quality inspection. We used a standard feature-based registration process in this investigation, but this does not preclude others to focus on the design and development of a new registration approach.

3.3 Multiresolution Analysis of Additive Manufacturing Imaging Data. Advanced imaging provides abundant process information, but calls upon an effective representation of image profiles to reveal the hidden defect patterns. Because defect characteristics are often buried in a single-scale view, traditional methods tend to be limited in the ability to handle multiscale patterns in image profiles. Wavelet transform is an effective tool for multiresolution analysis, which can resolve this issue by highlighting hidden information using mathematical transformations. However, few, if any, of the previous approaches utilized wavelet transformation for multiresolution inspection of layerwise AM contact images and in situ characterization of defect patterns.

As shown in Fig. 7, an image profile **s(x)** shows complex-structured patterns in the original scale, which pose significant challenges on the characterization and quantification of defects. Multiresolution analysis decomposes this image profile into various scales with wavelet lenses (i.e., scaling and convolution functions). In other words, each wavelet lens helps zoom into the image at a different scale. The patterns in the original scale are then decomposed into different scales, e.g., transformed images in six

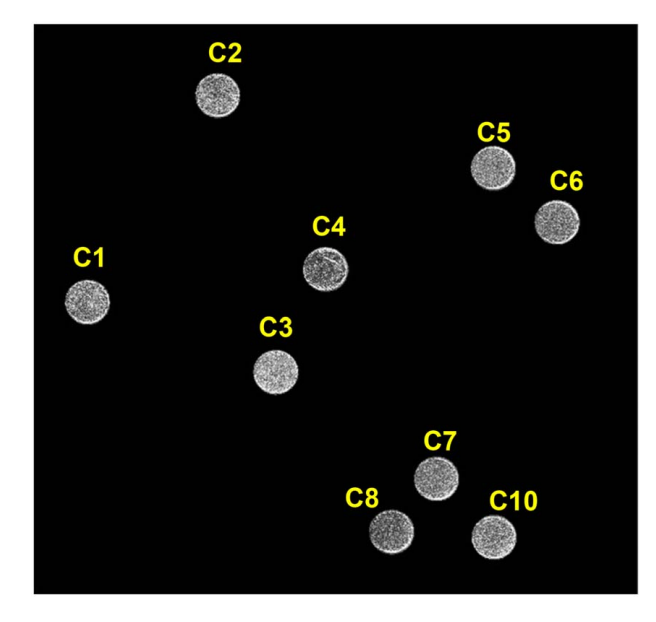


Fig. 6 Illustration of image registration and ROI segmentation

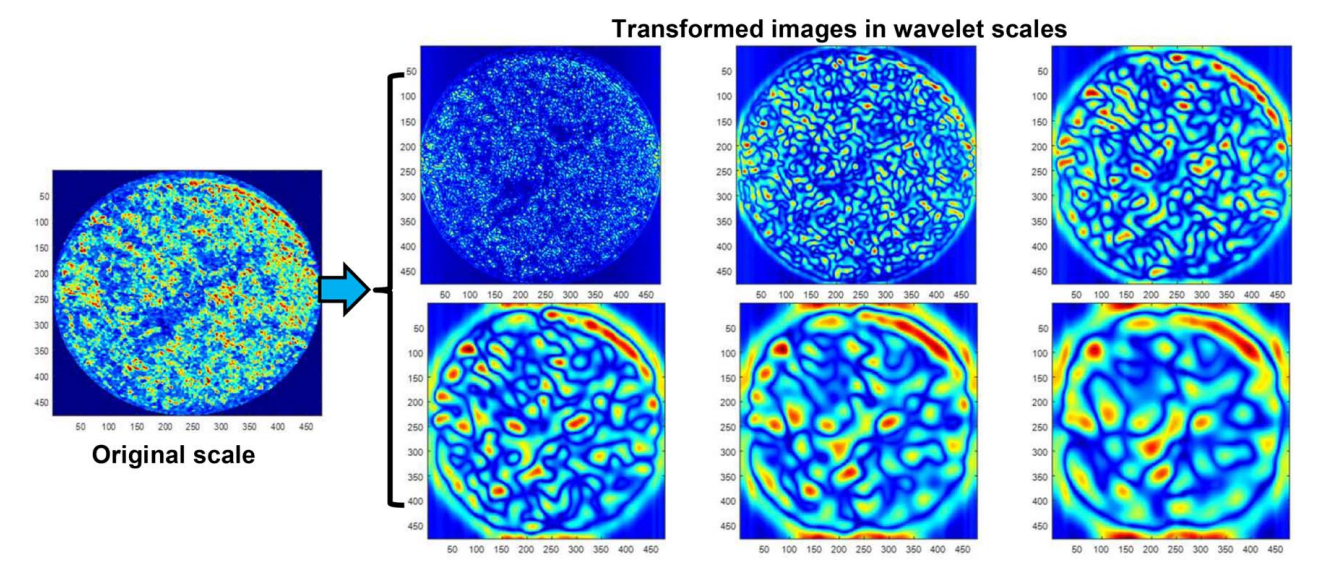


Fig. 7 Illustration of 2D continuous wavelet transformation of an image profile

wavelet scales in Fig. 7. As a result, this greatly facilitates the filtering and separation of low-frequency (i.e., steady trends), medium-frequency, and high-frequency (i.e., transient and noisy behaviors) patterns in the original image.

As opposed to the signal-scale analysis, wavelet transform provides a higher level of flexibility for multiresolution quality inspection. Therefore, this article presents multiresolution analysis of layerwise contact images to reveal hidden defects that cannot be discerned in the original scale. Note that traditional single-resolution analysis only uses the original images, while the multiresolution analysis examines the original images from multiple scales. This is different from the magnification into different scales. Single-resolution is a subset (or a part) of multiresolution. In other words, single resolution is included in the multiresolution analysis. Therefore, multiresolution analysis is guaranteed to be no worse than the single-resolution analysis.

In this investigation, 2D continuous wavelet transform (CWT) is used to delineate the defect characteristics in various frequency bands. The 2D CWT utilizes three mathematical operations—scaling, translation, and convolution—to obtain a space-scale representation of the image profile. The mother wavelet is a locally supported prototype function. Figure 8 illustrates the 2D Mexican hat function, which is defined as follows:

$$\psi(x, y) = -2\pi(x^2 + y^2) \exp\left(-\frac{(\sigma_x x)^2 + (\sigma_y y)^2}{2}\right), \quad \sigma_x \cdot \sigma_y \in \mathbb{R} \quad (1)$$

All wavelet functions are obtained by translating (shifting) and/or scaling the mother wavelet function. Let's define the position

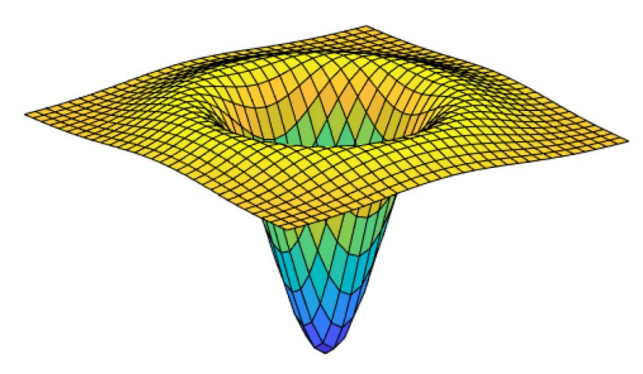


Fig. 8 Illustration of 2D mexh function

 \mathbf{x} is a 2D vector with real values (x, y), the image profile is $\mathbf{s}(\mathbf{x}) \in L^2(\mathbb{R}^2)$, a is a scaling factor that is a scalar, and \mathbf{b} is the translating factor that is a 2D vector. A mother wavelet function can be scaled as $\psi(\mathbf{x}) \to \psi(\mathbf{x}/a)$. If 0 < a < 1, then this is a contraction. If a > 1, then this becomes a dilation or expansion. In addition, the mother wavelet function can be translated to a new location as $\psi(\mathbf{x}) \to \psi(\mathbf{x} - \mathbf{b})$. As such, the mother wavelet at the scale a, at the translated location of \mathbf{b} is given as follows:

$$\psi_{a,\mathbf{b}}(\mathbf{x}) = \frac{1}{\sqrt{a}} \psi\left(\frac{\mathbf{x} - \mathbf{b}}{a}\right) \tag{2}$$

The 2D CWT of an AM image s(x) is defined as follows:

$$CWT_{s}^{\psi}(a, \mathbf{b}) = \int_{\mathbb{R}^{2}} s(\mathbf{x}) \psi_{a, \mathbf{b}}^{*}(\mathbf{x}) dx$$
$$= \int_{\mathbb{R}^{2}} s(\mathbf{x}) \frac{1}{\sqrt{a}} \psi^{*} \left(\frac{\mathbf{x} - \mathbf{b}}{a} \right) dx, \ a \in \mathbb{R}, \mathbf{x}, \mathbf{b} \in \mathbb{R}^{2} \quad (3)$$

In the L^2 space, an inner product is defined as $\langle s(\mathbf{x}), \psi_{(a,\mathbf{b})}(\mathbf{x}) \rangle = \int s(\mathbf{x}) \psi_{a,\mathbf{b}}^*(\mathbf{x}) \, \mathrm{d}x$. The wavelet transform is the inner product of the image profile with the mother wavelet at the scale a, at the translated location of \mathbf{b} . The scale factor a represents the extent to which we zoom-in or zoom-out an image. In other words, the inverse of the scale can be treated as a frequency variable. The translating factor \mathbf{b} represents the location where we perform the convolution or inner product between the image and the wavelet function. As a result, 2-D CWT $CWT_s^{\psi}(a, \mathbf{b})$ is a space-frequency representation that can be used to delineate the defect characteristics in various frequency bands.

3.4 Feature Extraction and Linear Mixed-Effects Modeling for Defect Prediction. As shown in Fig. 7, 2D CWT brings a series of transformed images at six different wavelet scales. These images show distinct and irregular patterns that capture transient, intermittent, or steady variations in the original AM image. Next, it is imperative to extract features to characterize and quantify the wavelet-scaled patterns. In this investigation, we extract the measures of central tendency, dispersion, and distribution shapes in each image, namely mean, min, max, standard deviation, kurtosis, and skewness. In total, multiresolution analysis leads to a high-dimensional feature space (i.e., $6 \times 6 = 36$ features when six features are extracted in each of six wavelet scales). As such, there is a need to avoid the issue of "curse of dimensionality" for the predictive modeling. In other words, it is desirable to build a sparse model

Gas flow
Part(s) 2. 17421.102 mm3

Omnorpul rescontor Alberta

Discontract and the second of the sec

Fig. 9 Build layout and pictures of sample builds in the real-world case study

1.

Blocked gas flow nozzles

to predict the level of defects. Such a sparse model should include a parsimonious set of parameters and prevents the overfitting, while maintaining the prediction performance.

Therefore, we further leverage the PCA to reduce the dimensionality of features. Note that PCA orthogonalizes the set of features to reduce mutual correlations, and orders the resulting PCs from the largest variation to the smallest. The PC is a linear combination of wavelet features. In this process, PCA does not discard some features or retain other features, but rather identify the largest variance or the second largest variance in the feature set. The set of raw features is transformed into a sparse set of PCs by reducing mutual correlations and projecting out redundant information. An effective PCA transformation often provides a smaller set of PCs to capture a large percentage of variances (>90%) in the feature datasets. These PCs are also more sensitive to AM process changes later in the section of experimental results. Because these PCs are orthogonal and uncorrelated, this also facilitates the construction of linear mixed-effects models for the prediction of defect levels.

In this investigation, contact images are collected from nine parts in the same building plate. Each AM part is treated with different levels of experimental factors (i.e., gas flow, laser power, re-coater blade scratch). As a result, wavelet features are extracted and

Table 1 Factor levels for sample builds in the real-world case study

Ajo#	Laser power W	Factor levels
C1	200	Nominal reference with a nearby C9
C2	200	Nominal reference (no nearby samples)
C3	100	Low laser power
C4	300	High laser power
C5	200	Scratches on re-coater blade
C6	200	Scratches on re-coater blade
C7	200	Blocked gas flow
C8	200	Blocked gas flow
C9	200	None, just a dummy piece
C10	200	Blocked gas flow (and scratches on re-coater blade)

Note: Scanning speed is 800 mm/s, and hatch distance is 0.12 mm for all parts.

organized into nine groups (i.e., each AM part is a group). Traditional regression models overlook this grouping variable and cannot adequately handle the feature datasets that are summarized in groups. Linear mixed-effects models are commonly utilized to handle grouped data, where model parameters are allowed to vary with respect to grouping variables. Hence, we propose to develop a linear mixed-effects model to predict the defects as follows:

Aio 460

$$y = X\beta + Zb + \epsilon \tag{4}$$

$$y_{im} = x_{im}^T \beta_i + Z_{im}^T b_{im} + \epsilon_{im}, i = 1, 2, ..., n; m = 1, 2, ..., M$$
 (5)

where y is the dependent variable (i.e., the level of defects), n is the total number of layers for nine parts, m is the grouping variable with M levels (i.e., M=9), X is the fixed-effects variables (i.e., three PCs, laser power, gas flow, re-coater damage), Z is the random-effects variables (i.e., laser power), and ε is random errors. Note that this model is composed of two parts, fixed effects $X\beta$, and random effects Zb. Random effects are pertinent to nine AM parts, where each part is an experimental unit. Random-effects coefficients b_{im} can vary with respect to the experimental unit (or a grouping variable) and are independent from random errors ε . This mixed-effects models effectively handle the covariance structure pertaining to the grouping of feature datasets.

4 Experimental Design

The proposed methodology is evaluated and validated with real-world experimental data (i.e., CIS imaging data, CT scans) from nine parts fabricated in a SLM125 machine. Figure 9(a) shows the layout of nine parts in the build plate, each of which is treated with a different combination of factor levels. Figure 9(b) shows the picture of nine parts after the AM building process is completed. Note that there are two horns in these parts, which are used for the positioning purpose of layers in the CT scans. The horn angles and locations are designed so that one-to-one correspondence can be derived between CIS images and CT scans. As shown in Fig. 9(a) and Table 1, experimental factors include changes in laser power (i.e., 100 W, 200 W, and 300 W), scratches on the re-coater blade, and the blockage of gas flows. The scanning speed is holding constant as 800 mm/s, and hatch distance is 0.12 mm for all the nine parts. Argon was used as shielding gas, and

the layer thickness was 30 μ m for the build. The hypotheses to be tested are as follows: (1) whether and how the changes of factor levels lead to the quality issues in the final builds? (2) whether multiresolution analysis of CIS images is capable of capturing and predicting the quality variations in final builds? Addressing these research questions is critical to designing a new sensor-based approach for in situ quality monitoring of AM processes, thereby mitigating scrap and rework rates and further increasing the high-quality throughput of AM.

5 Experimental Results

5.1 Principal Component Analysis of Wavelet Features. Multiresolution analysis provides an opportunity to zoom in and out of a layerwise image to capture microlevel fine-grained details and macrolevel approximations of surface finishes in each layer of the AM build. On the other hand, this leads to multiple zoom-in and zoom-out images with different wavelet lenses. As discussed in Sec. 3.4, we extract the statistical features of central tendency, dispersion, distribution shapes in each image, namely, mean, min, max, standard deviation, kurtosis, and skewness. In the present article, multiresolution analysis is performed with six wavelet lenses that lead to a total $6 \times 6 = 36$ features for each layer. However, a predictive model with 36 features tends to be complex and prone to overfitting. In contrast, we propose to reduce the dimensionality of features into a sparse set of salient principal components that preserve the information in the feature space. PCA computes the variance-covariance structure underlying the original data, and then performs eigen decomposition to identify the directions of eigenvectors. As such, PCA facilitates the interpretation of data along the eigenvector directions, each of which provides useful information about the data variances.

As shown in Fig. 10(a), the first two PCs capture approximately 80% variances in the feature datasets, while the first three PCs capture roughly 91.06% variances. In other words, if only the first three PCs are kept, we can approximately project out redundant information and reconstruct 91.06% of original features. Note that PCA does not discard some features or retain other features, but rather transforms raw features into PCs along the directions of the largest variations or the second largest variations. Therefore, we will use the first two and/or three PCs in the following sections to show how they are related to the changes of factor levels in the experiments. Figure 10(b) shows the scatter plot of the first two PCs for nine parts, each of which is represented with a different colored marker. For example, blue upper triangles represent all layers from the part C3 that is built with a low laser power 100 W. It may be noted that these blue triangles are away from clusters of other parts. In particular, red circles denote the layers from the part C4 that is built with a high laser power 300 W. Although C3 and C4 can be seen to be separated from other parts. There are also other changes in the factor levels such as scratches on the re-coater blade, gas flow blockage) mixed in the nine parts. Hence, we will perform two-group or three-group comparison analysis in Sec. 5.2 to study whether and how wavelet features are sensitive to AM process changes.

5.2 Paired Comparison Analysis. First, both parts C1 and C2 are nominal references, but their locations are different in the build plate and C1 is next to a nearby dummy piece C9. This dummy piece is designed to generate fumes to neighboring parts. Figure 11(a) shows the 2D scatter plot of parts C1 and C2. Most of the layers are mixed with each other, and there are no significant separations from the parts C1 to C2. This is mainly due to the fact that both parts are nominal pieces and are not treated with the changes of factor levels as other parts. However, the 3D scatter plot in Fig. 11(b) shows that these two parts are slightly separated from each other, albeit not as significant as the change of laser powers in parts C3 and C4. However, these slight differences may be due to other factors (e.g., the fumes, locations) and can

be used to further predict the incipient variations of quality (or defect levels) in the final build.

Second, Fig. 12 shows that the part C3 is significantly separated from C4 in both 2D and 3D scatter plots. This is mainly due to the fact that C3 and C4 are treated with two different levels of laser powers 100 W and 300 W, respectively. However, high laser power 300 W on C4 is shown to cause more variations in the PCs of wavelet features. Low laser power 100 W produces the layers of C3 that are closely clustered in a smaller region. In order to examine the differences from a nominal reference, we have also added C2 into the 2D and 3D scatter plots, as shown in Fig. 13. Note that C2 is treated with laser power 200 W and is shown in the middle section between C3 and C4. Collectively, these figures demonstrate that wavelet features from layerwise CIS images are sensitive to the variations of laser powers.

Third, Fig. 14(a) shows the 2D scatter plot of the first two PCs for parts C2, C5, and C6. Note that C5 and C6 are located in the area of build plate where re-coater blade is damaged (i.e., artificially created). The purpose to create distortions in the spread of powders to C5 and C6. However, there are no significant separations for these three parts in the 2D plot. This is mainly due to the fact that the damages to re-coater blade are not noticeable when cut with a sharp knife after re-examining the re-coater. In the experiments, it was found that there are not significant distortions in the spread of powders over the C5 and C6 area. On the contrary, C5 and C6 yield approximately the same quality in the final builds. In the future work, we plan to avoid this oversight and create larger and more noticeable damages to the re-coater blade. Despite this failure, the 3D scatter plot of the first three PCs shows that C5 and C6 are closely mixed with each other, while C2 is slightly away from them (also see Fig. 14(b)). Indeed, experimental results showed that there are slight differences in the quality (or defect levels) from the CT scans of final builds.

Finally, Fig. 15 shows the 2D and 3D scatter plots of PC features for parts C2 (no gas flow blockage) versus C7, C8, and C10 (with gas flow blockage). Similarly, it was expected that the blockage of gas flows impacts the cooling and thermal distributions and the extraction of fumes/spatters in the build plate area of C7, C8, and C10. However, Fig. 15 shows that these parts are not significantly separated from the nominal reference C2. After re-examining the blockage, we found that gas flow nozzles on this areas are were effectively blocked during the experiment. Nonetheless, SLM125 AM machine has a nominal building platform of 125 × 125 mm, which is a relatively small area. As shown in Fig. 9, gas flows from the upper 3/4 area can effectively circulate and spread to the blocked 1/4 area of C7, C8, and C10. As such, parts C7, C8, and C10 yield approximately the same quality as C2 in the final builds. Overall, experimental results show that wavelet features and PCs are salient and sensitive to AM process changes. This investigation will further leverage the first three PCs to build a sparse predictive model for the prediction of defect levels in the final AM builds.

5.3 Computed Tomography Defect Quantification. In this investigation, we also performed CT scans of all the nine parts that are treated with different factor levels. GE Phoenix vltomelx CT scanner was used, and CT data were acquired with $12 \,\mu m$ voxel resolution. Because the part can be rotated, titled, or flipped during the CT scanning, we design the horns on the top of each cylindrical part to establish one-to-one correspondence between CIS images and CT scans (i.e., also discussed in Sec. 4).

In order to characterize the defect level, each layer of the CT scan is processed as follows: (1) *Identify the circular ROI*: As shown in Fig. 16(a), each layer of the CT scan is a square-sized image, but the cylindrical part is situated within a circular ROI. Thus, the first step is to create a circular mask on the ROI because there are noises and other nuances outside the ROI. (2) *Binary masking*: The second step is to create a binarized mask, i.e., ones inside the ROI and zeros outside the ROI. Then, we apply the binarized mask to the original

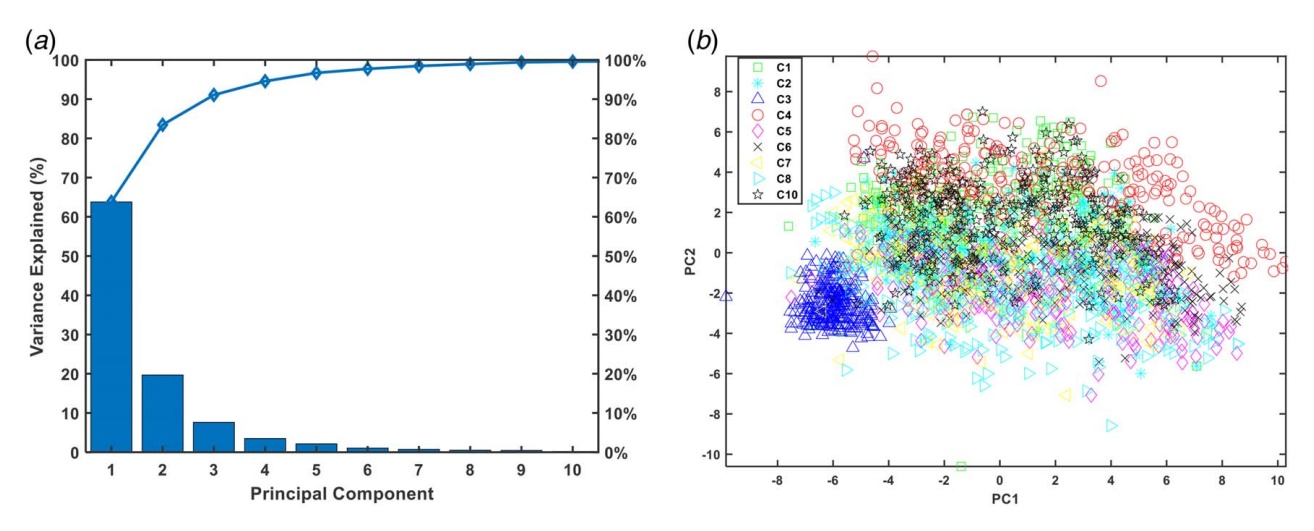


Fig. 10 (a) Variance explained with respect to the number of PCs and (b) scatter plot of the first two PCs for nine AM parts (Color version online.)

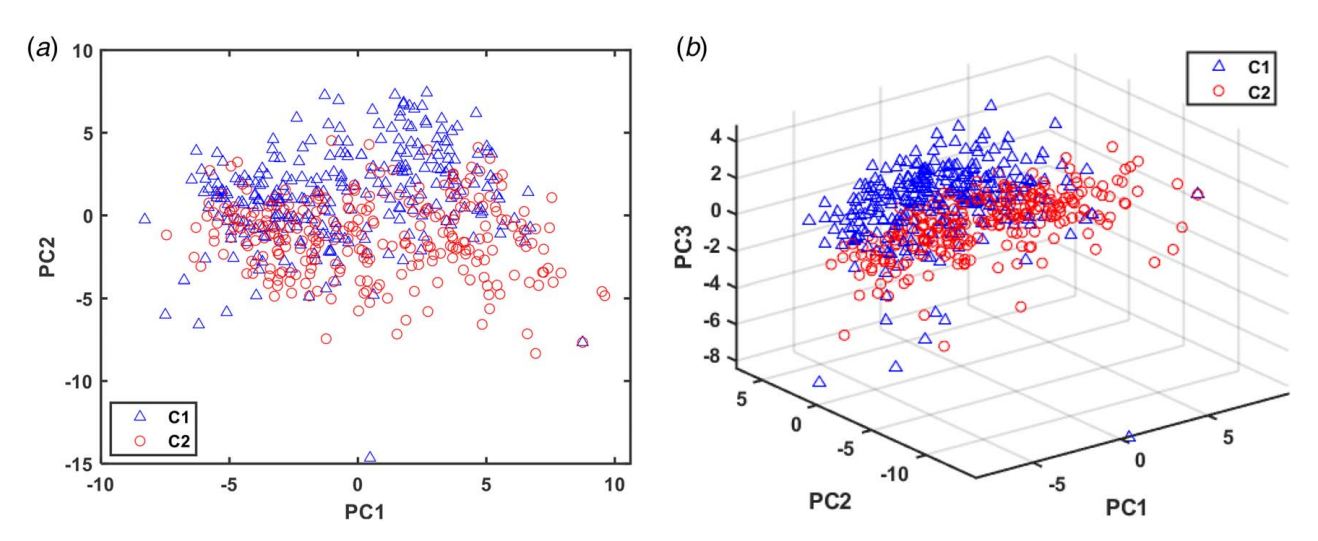


Fig. 11 (a) 2D and (b) 3D scatter plots of PCs for parts C1 and C2 (i.e., nominal references) (Color version online.)

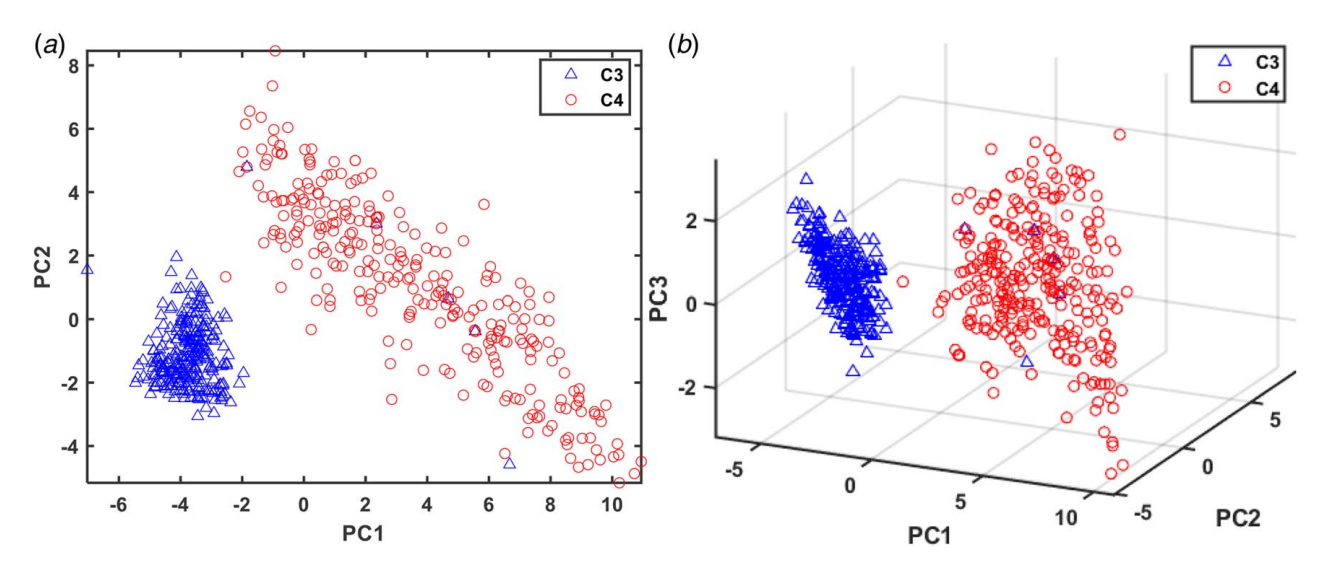


Fig. 12 (a) 2D and (b) 3D scatter plots of PCs for parts C3 (laser power 100 W) and C4 (laser power 300 W)

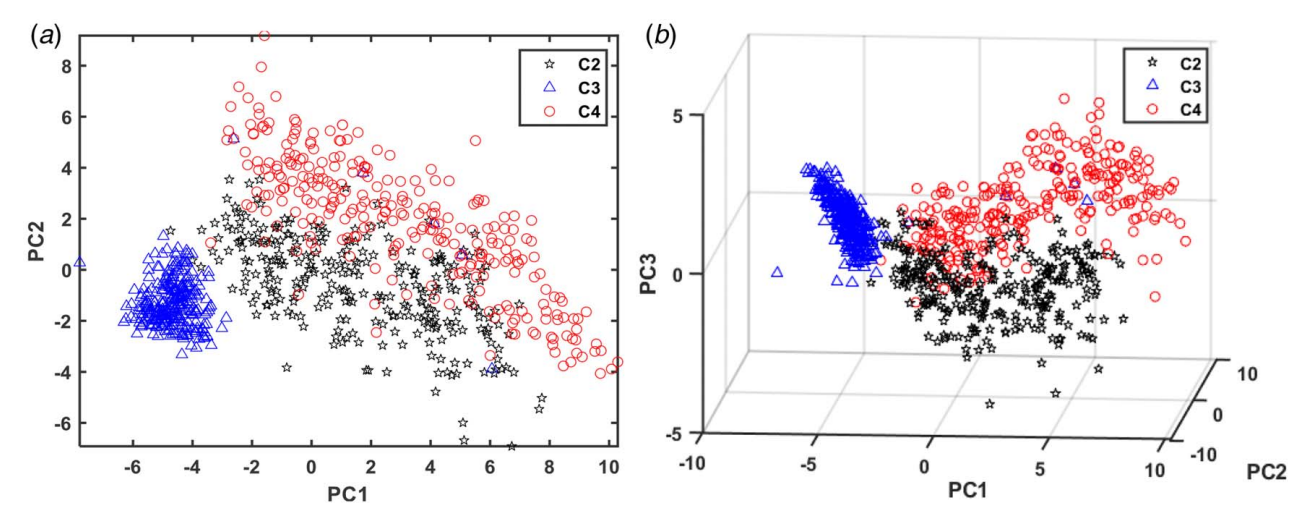


Fig. 13 (a) 2D and (b) 3D scatter plots of PCs for parts C2 (laser power 200 W), C3 (laser power 100 W), and C4 (laser power 300 W)

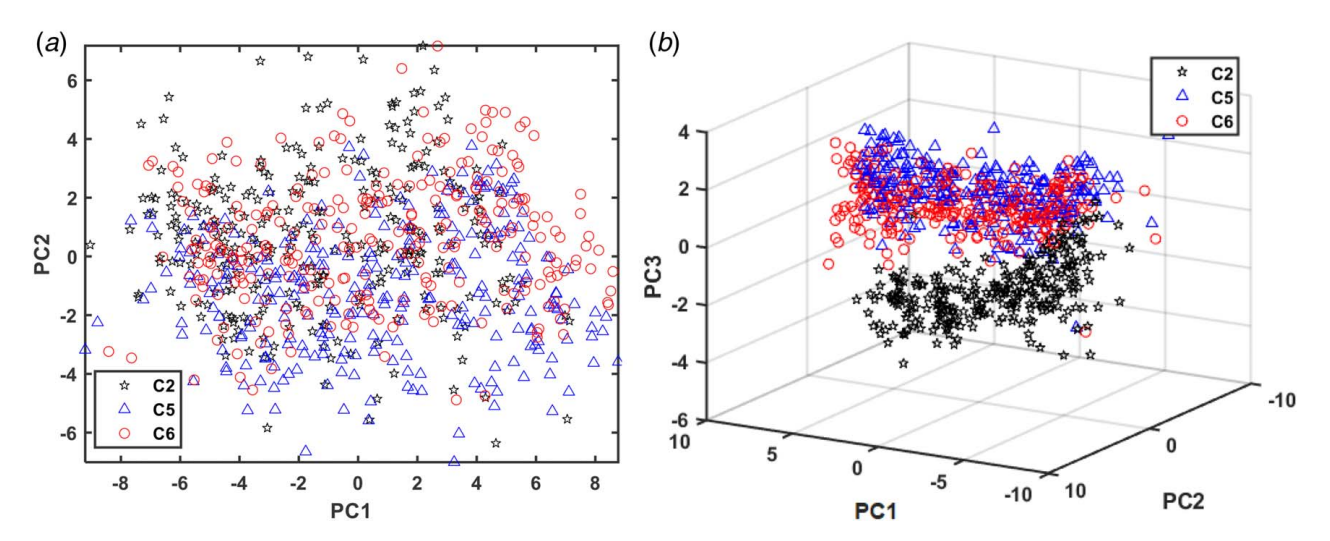


Fig. 14 (a) 2D and (b) 3D scatter plots of PCs for parts C2 (no scratches on the re-coater blade) versus C5 and C6 (with scratches on the re-coater blade)

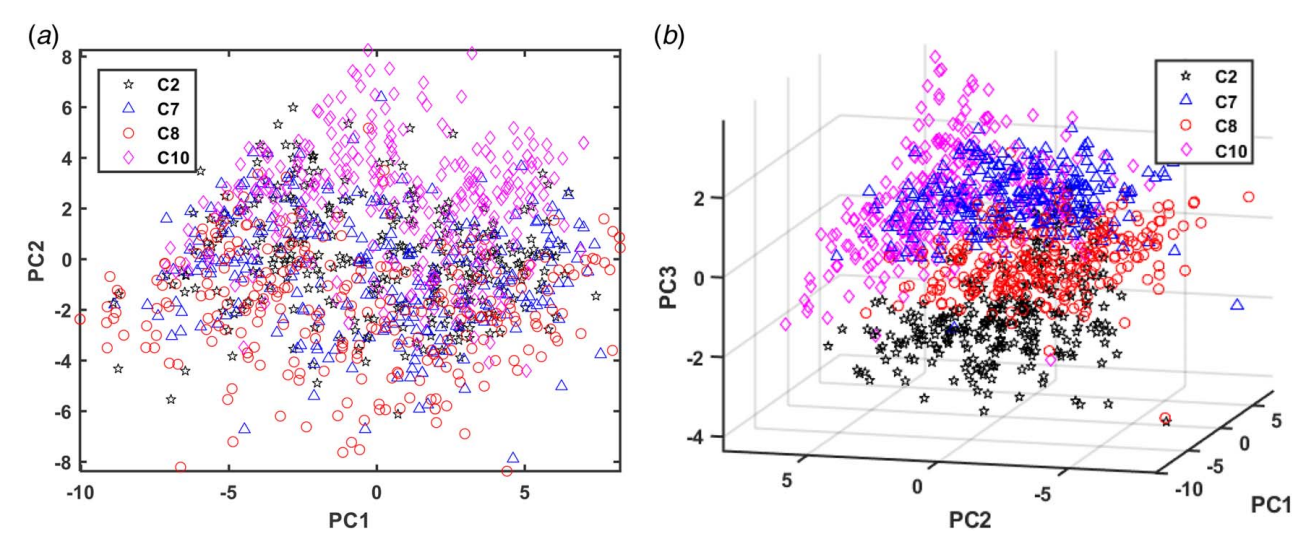


Fig. 15 (a) 2D and (b) 3D scatter plots of PCs for parts C2 (no gas flow blockage) versus C7, C8, and C10 (with gas flow blockage)

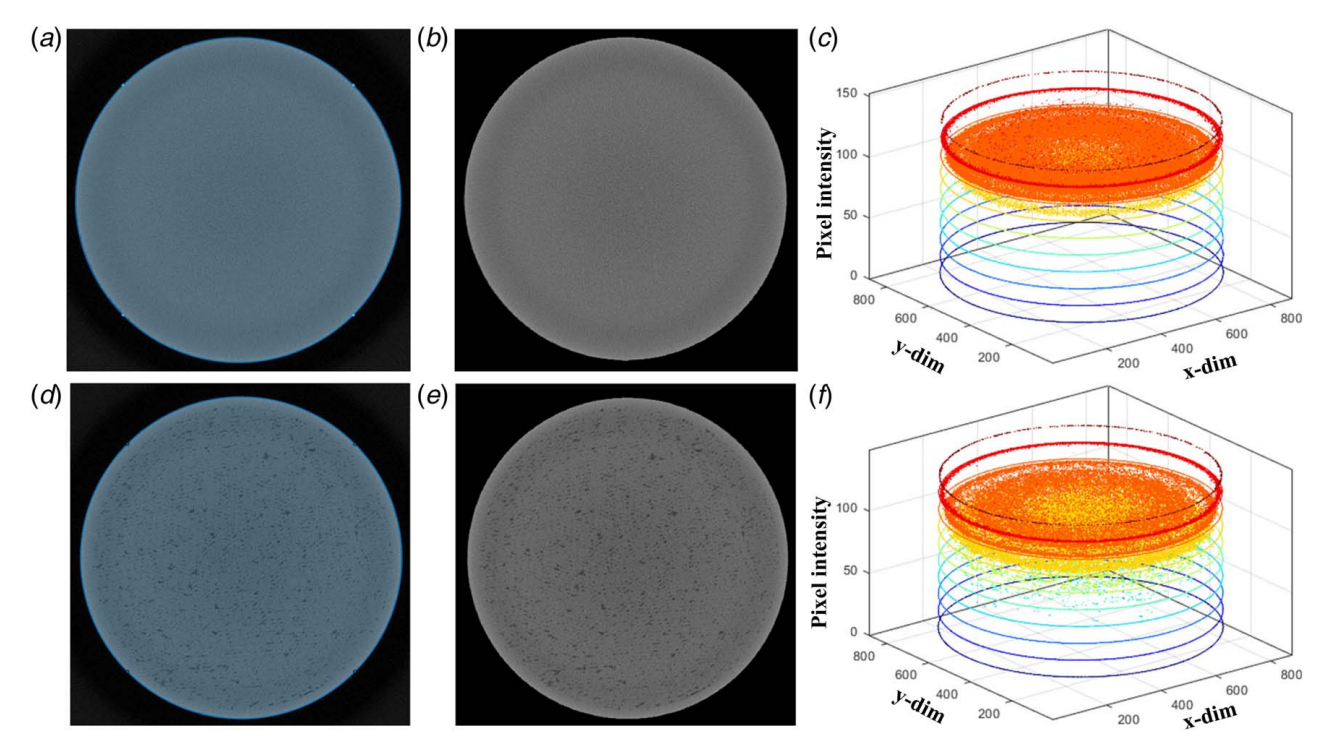


Fig. 16 (a) Circular ROI, (b) masked CT scan, and (c) stratified contour plot for a high-quality layer, (d) circular ROI, (e) masked CT scan, and (f) stratified contour plot for a low-quality layer. Note: In the stratified contour plot, X-axis is the x-dimension of the CT image (i.e., image size along the x dimension); Y-axis is the y-dimension of the CT image (i.e., image size along the y-dimension); and Z-axis is the pixel intensity contours of the CT image.

CT scan to get the noise-free ROI, as shown in Fig. 16(b). Although the regions outside the ROI seem to be the same as black as before in Fig. 16(a), noises in low-intensity values are already cancelled. (3) Stratified contours: In the third step, pixel values within the ROI are stratified into ten contours, as shown in Fig. 16(c). The idea behind is to characterize the level of darker pixels within the circular ROI. Note that defects tend to yield darker pixel values than nondefects. As shown in Figs. 16(d)–16(f), a lowquality layer with porosities tends to have more pixels distributed in the bottom four contours. However, the high-quality layer has fewer pixels in the bottom four contours. The top two layers approximately correspond to the cupping effect due to the beam hardening of the x-ray. (4) CT defect characterization: In this investigation, pixel values are stratified into ten contours within the ROI for each layer of the CT scan. The defect level is characterized as the ratio of pixels that fall into the bottom four contours. In other words, the defect level is the percentage of darker pixels (i.e., in the bottom four levels of contours) with respect to all pixels in each layer of the CT scan. As such, the defect level is characterized as a continuous variable (i.e., using the ratio as a general descriptor of pixel irregularity in this case study), as opposed to a discrete variable (i.e., defect or not, or low, medium, high). Therefore, predictive modeling in the next section becomes a regression problem instead of a classification problem.

5.4 Predictive Modeling. In situ contact images are collected from nine parts in the same build plate. Each part serves as a group variable of wavelet features, which are extracted from layerwise images during the AM process. If this grouping variable is overlooked, traditional regression models cannot adequately handle the feature datasets that are summarized in groups. Therefore, as discussed in Sec. 3.4, we propose linear mixed-effects models to handle grouped data in this investigation, where random-effect parameters are allowed to vary with respect to grouping variables. Specifically, the response variable is the defect level which is

quantified from CT scans. Each part serves as the grouping variable, fixed-effects variables are three PCs, laser power, gas flow, re-coater damage, and the random-effects variable is laser power.

As shown in Fig. 17(a), there are a total of 2511 layerwise images included for the in situ prediction of quality in nine parts (i.e., marked as C1, C2, C3, ..., C10), each of which contains 279 layers. The idx numbering corresponds to the cumulative layers for each of the parts, e.g., layer 280 corresponds to layer 1 of the second part. The defect levels from CT scans are marked as gray data points, while predictions from linear mixed-effects and fixed-effects models are marked as blue and red lines, respectively. Note that linear mixed-effects models yield better performance to predict the defect levels than the fixed-effects models. This is mainly due to the fact that mixed-effects models leverage the random-effect parameters to account for different variances in each part. Figure 17(a) shows that the variances of defect levels are different for each part. For example, C2 as a nominal reference yields a smaller level of variances across its 279 layers, but C3's variances are much higher. The fixed-effects models do not account for such differences in variances for each part. Therefore, such variations are included as a part of prediction results. This is also the reason why predictions from fixed-effects models (red lines) tend to have higher oscillations than mixed-effects models (blue lines) in Fig. 17(a). Overall, we found that C3, C4, and C8 yield higher defect levels than the rest of six parts.

Figure 17(b) shows the visualization of residuals versus fitted values for the linear mixed-effects model. This residual plot provides the model diagnosis results, which show no systematic patterns of linear or nonlinear trends left in the residuals and show only parallel bands centered around zero. Figure 17(c) shows the histogram plot of the residuals from the linear mixed-effects model, which is normally distributed around zero. These results validate the normality assumption of residuals. In addition, it should be noted that the results of predictive models are consistent with the

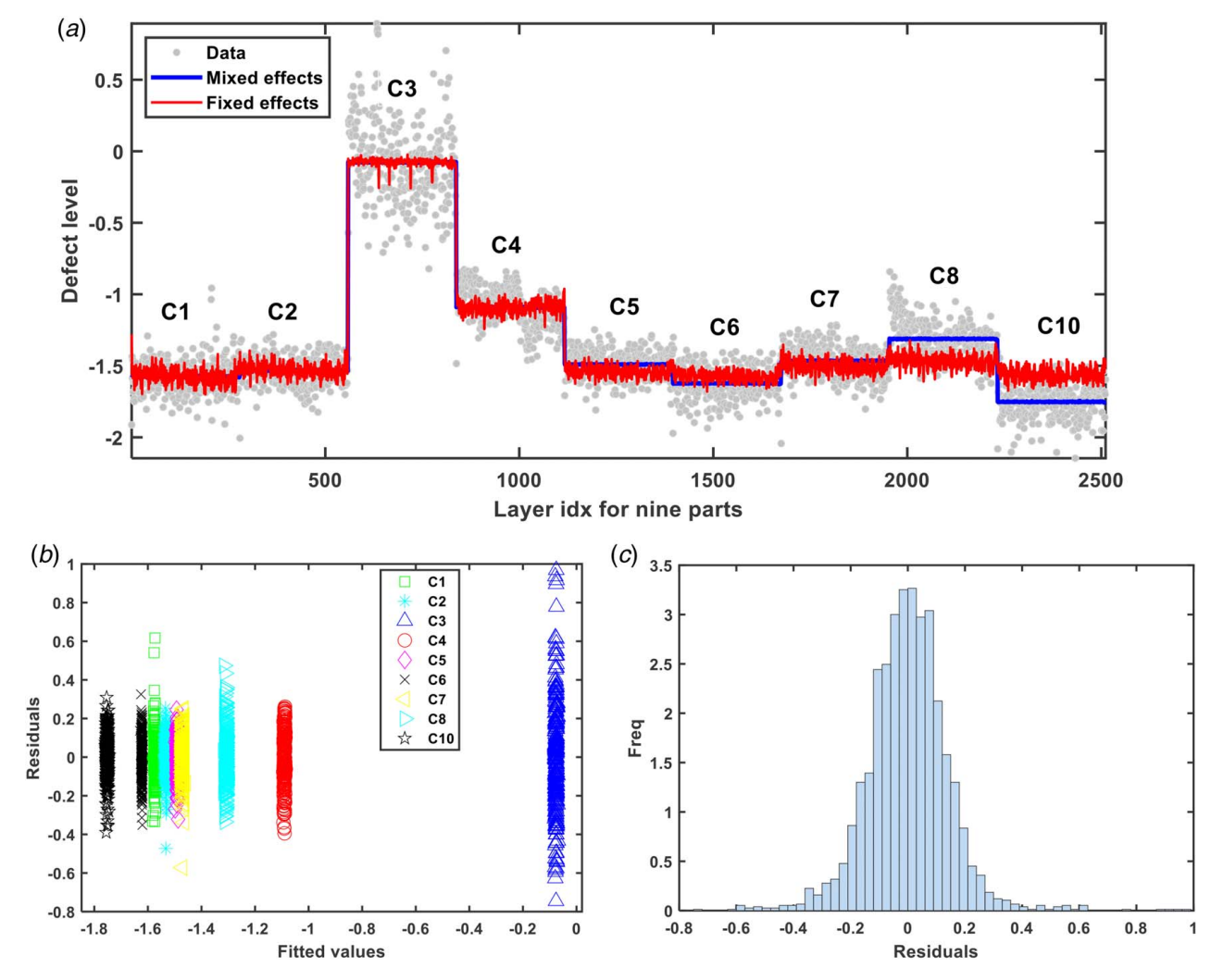


Fig. 17 (a) Goodness-of-fit of mixed-effects versus fixed-effects models, (b) plot of residuals versus fitted values of mixed-effects model, and (c) histogram plot of residuals from nine parts (Color version online.)

paired comparison analysis, showing that wavelet features and PCs are salient and sensitive to AM process changes.

6 Conclusions

Additive manufacturing is strongly promised to revolutionize the next generation of production paradigms and provide higher flexibility in the supply chain configurations. Although there are significant advances to equip AM machines with in situ sensing systems, few, if any, have investigated the capability of high-speed CIS sensors (i.e., originally developed for document scanners and multifunction printers) for in situ quality inspection during the AM processes. In this article, we develop a multiresolution quality inspection framework toward an integrated metal 3D printer and scanner. The layerwise scanning is realized by retrofitting a CIS sensing and data acquisition system into the LPBF-AM machine.

This, in turn, brings large amounts of layerwise imaging data, which are complex structured and often contain nonlinear, nonstationary, and irregular patterns. Most of the existing works tend to focus on image processing and analysis in a single scale. It is not uncommon that the progressive formation of defects is often buried in such a single-scale view. Therefore, this paper focuses on the development of an AOI system with CIS for multi-resolution quality inspection of layerwise builds in additive manufacturing. Experimental results of paired comparison analysis show that wavelet transformation effectively captures microlevel fine-grained

details and macrolevel approximations of ROI images in multiple scales and further helps extract salient features that are sensitive to process variations, instead of extraneous noises. Further, as opposed to traditional regression models overlooking the grouping effects, linear mixed-effects models effectively account for the grouping variable in each part and yield better performance to predict the defect levels than the fixed-effects models.

High-fidelity quality monitoring is critical to promoting widespread applications of AM in the industry. The provision of new sensor-based quality technologies to AM manufacturers increases their competitive advantage in the global market. Sensor-based quality monitoring is conducive to mitigating scrap and rework rates and further ensuring economic viability of AM. As opposed to traditional single-scale inspection, the proposed multiresolution QA/QC has the potential to substantially improve repeatability and reliability of functional integrity aspects in metal AM.

Finally, this investigation is aimed at building the predictive model from CIS imaging data to defect measures in CT scans at each layer of AM process. In the future work, it is worth investigating neighboring effects among adjacent layers. When defects occur, sometimes they cannot be captured as soon as the laser scans over a localized spot, but rather evolve dynamically to their size after rescanning. Our previous studies have developed statistical models of layerwise-dependent effects in the evolving dynamics of defect formations, albeit from on-axis melt-pool images [22–24]. In addition, it is worth investigating the link between the physical influence and changes with each experimental condition and the

PCA analysis. There are also acoustic emission and melt-pool signals collected simultaneously in the LPBF-AM process. Our future work will focus on the investigation of physical influences, as well as multisensor integration for AM process monitoring.

Acknowledgment

H.Y. thanks Fulbright Finland Foundation and VTT Technical Research Center for financial support to this research. We gratefully acknowledge the valuable contributions of VTT team of advanced manufacturing technologies (especially Kimmo Ruusuvuori) for carrying out the experiments and providing the data utilized in this research. We are grateful to Jukka Kuva from GTK Finland for conducting the CT scanning.

Conflict of Interest

There are no conflicts of interest.

Data Availability Statement

The datasets generated and supporting the findings of this article are obtainable from the corresponding author upon reasonable request.

References

- Abdelrahman, M., Reutzel, E. W., Nassar, A. R., and Starr, T. L., 2017, "Flaw Detection in Powder Bed Fusion Using Optical Imaging," Addit. Manuf., 15, pp. 1–11
- [2] Imani, F., Gaikwad, A., Montazeri, M., Rao, P., Yang, H., and Reutzel, E., 2018, "Layerwise In-Process Quality Monitoring in Laser Powder Bed Fusion," 13th International Manufacturing Science and Engineering Conference, Vol. 51357, College Station, TX, June 18–22, American Society of Mechanical Engineers, p. V001T01A038.
- [3] Yang, Z., Lu, Y., Yeung, H., and Krishnamurty, S., 2020, "From Scan Strategy to Melt Pool Prediction: A Neighboring-Effect Modeling Method," ASME J. Comput. Inf. Sci. Eng., 20(5), p. 051001.
- [4] Yang, Z., Lu, Y., Li, S., Li, J., Ndiaye, Y., Yang, H., and Krishnamurty, S., 2021, "In-Process Data Fusion for Process Monitoring and Control of Metal Additive Manufacturing," International Design Engineering Technical Conferences and Computers and Information in Engineering Conference, Vol. 85376, Virtual, Online, Aug. 17–19, American Society of Mechanical Engineers, p. V002T02A072.
- [5] Khanzadeh, M., Chowdhury, S., Tschopp, M. A., Doude, H. R., Marufuzzaman, M., and Bian, L., 2019, "In-Situ Monitoring of Melt Pool Images for Porosity Prediction in Directed Energy Deposition Processes," IISE Trans., 51(5), pp. 437–455.
- [6] Yao, B., Imani, F., and Yang, H., 2018, "Markov Decision Process for Image-Guided Additive Manufacturing," IEEE Rob. Autom. Lett., 3(4), pp. 2792–2798.
- [7] Lane, B., Mekhontsev, S., Grantham, S., Vlasea, M. L., Whiting, J., Yeung, H., Fox, J., Zarobila, C., Neira, J., McGlauflin, M., and Hanssen, L., 2016, "Design, Developments, and Results From the Nist Additive Manufacturing Metrology Testbed (AMMT)," 2016 International Solid Freeform Fabrication

- Symposium An Additive Manufacturing Conference, Austin, TX, Aug. 8–10, University of Texas at Austin.
- [8] Lane, B., Moylan, S., Whitenton, E. P., and Ma, L., 2016, "Thermographic Measurements of the Commercial Laser Powder Bed Fusion Process at NIST," Rapid. Prototyp. J., 22(5), pp. 778–787.
- [9] Nassar, A. R., Reutzel, E. W., Brown, S. W., Morgan, J. P., Jr, Morgan, J. P., Natale, D. J., Tutwiler, R. L., Feck, D. P., and Banks, J. C., 2016, "Sensing for Directed Energy Deposition and Powder Bed Fusion Additive Manufacturing at PENN State University," Laser 3D Manufacturing III, Vol. 9738, San Francisco, CA, Apr. 6, SPIE, pp. 77–90.
- [10] Dunbar, A., Denlinger, E., Heigel, J., Michaleris, P., Guerrier, P., Martukanitz, R., and Simpson, T., 2016, "Development of Experimental Method for In Situ Distortion and Temperature Measurements During the Laser Powder Bed Fusion Additive Manufacturing Process," Addit. Manuf., 12(Part A), pp. 25–30.
- [11] Montazeri, M., Yavari, R., Rao, P., and Boulware, P., 2018, "In-Process Monitoring of Material Cross-Contamination Defects in Laser Powder Bed Fusion," ASME J. Manuf. Sci. Eng., 140(11), p. 111001.
- [12] Yang, H., Rao, P., Simpson, T., Lu, Y., Witherell, P., Nassar, A. R., Reutzel, E., and Kumara, S., 2020, "Six-Sigma Quality Management of Additive Manufacturing," Proc. IEEE, 109(4), pp. 347–376.
- [13] McCann, R., Obeidi, M. A., Hughes, C., Vijayaraghavan, R. K., Joshi, A. M., Garzon, V. A., Dowling, D. P., McNally, P. J., and Brabazon, D., 2021, "In-Situ Sensing, Process Monitoring and Machine Control in Laser Powder Bed Fusion: A Review," Addit. Manuf., 45(1), p. 102058.
- [14] Lu, Q., Grasso, M., Le, T.-P., and Seita, M., 2022, "Predicting Build Density in L-PBF Through In-Situ Analysis of Surface Topography Using Powder Bed Scanner Technology," Addit. Manuf., 51, p. 102626.
- [15] Le, T.-P., and Seita, M., 2019, "A High-Resolution and Large Field-of-View Scanner for In-Line Characterization of Powder Bed Defects During Additive Manufacturing," Mater. Des., 164, p. 107562.
- [16] Caggiano, A., Zhang, J., Alfieri, V., Caiazzo, F., Gao, R., and Teti, R., 2019, "Machine Learning-Based Image Processing for On-line Defect Recognition in Additive Manufacturing," CIRP. Ann., 68(1), pp. 451–454.
- [17] Yao, B., Imani, F., Sakpal, A. S., Reutzel, E., and Yang, H., 2018, "Multifractal Analysis of Image Profiles for the Characterization and Detection of Defects in Additive Manufacturing," ASME J. Manuf. Sci. Eng., 140(3), p. 031014.
- [18] Imani, F., Yao, B., Chen, R., Rao, P., and Yang, H., 2019, "Joint Multifractal and Lacunarity Analysis of Image Profiles for Manufacturing Quality Control," ASME J. Manuf. Sci. Eng., 141(4), p. 044501.
- [19] Kan, C., and Yang, H., 2017, "Dynamic Network Monitoring and Control of In Situ Image Profiles From Ultraprecision Machining and Biomanufacturing Processes," Qual. Reliab. Eng. Int., 33(8), pp. 2003–2022.
- [20] Imani, F., Chen, R., Diewald, E., Reutzel, E., and Yang, H., 2019, "Deep Learning of Variant Geometry in Layerwise Imaging Profiles for Additive Manufacturing Quality Control," ASME J. Manuf. Sci. Eng., 141(11), p. 111001.
- [21] Yazdi, R. M., Imani, F., and Yang, H., 2020, "A Hybrid Deep Learning Model of Process-Build Interactions in Additive Manufacturing," J. Manuf. Syst., 57, pp. 460–468.
- [22] Liu, R., Vogt, B. D., and Yang, H., 2021, "Gaussian Process Monitoring of Layerwise-Dependent Imaging Data," IEEE Rob. Autom. Lett., 6(4), pp. 8029– 8036
- [23] Yang, H., Zhang, S., Lu, Y., Witherell, P., and Kumara, S., 2022, "Spatiotemporal Monitoring of Melt-Pool Variations in Metal-Based Additive Manufacturing," IEEE Rob. Autom. Lett., 7(3), pp. 8249–8256.
- [24] Liu, R., and Yang, H., 2023, "Multimodal Probabilistic Modeling of Melt Pool Geometry Variations in Additive Manufacturing," Addit. Manuf., 61, p. 103375.
- [25] Yang, H., Bukkapatnam, S., and Komanduri, R., 2007, "Nonlinear Adaptive Wavelet Analysis of Electrocardiogram Signals," Phys. Rev. E, 76(2), p. 026214.
- [26] Yang, H., 2010, "Multiscale Recurrence Quantification Analysis of Spatial Cardiac Vectorcardiogram Signals," IEEE Trans. Biomed. Eng., 58(2), pp. 339–347.
- [27] Liu, G., and Yang, H., 2013, "Multiscale Adaptive Basis Function Modeling of Spatiotemporal Vectorcardiogram Signals," IEEE J. Biomed. Health Inform., 17(2), pp. 484–492.